RSC Advances

ROYAL SOCIETY OF CHEMISTRY

www.rsc.org/advances

Controllable Synthesis of Novel Hierarchical V_2O_5/TiO_2 Nanofibers with Improved Acetone Oxidation Performance

Xuecheng Zhu, Jinghuan Chen, Xinning Yu, Xinbo Zhu, Xiang Gao *, Kefa Cen

† *State Key Laboratory of Clean Energy Utilization, Zhejiang University, Hangzhou 310027, Zhejiang, China*

Abstract

A controllable strategy to fabricate novel hierarchical V_2O_5/TiO_2 nanofiber catalysts was proposed. The catalysts, which comprised primary TiO_2 nanofibers and secondary V_2O_5 nanoparticles, were fabricated by combining electrospinning and hydrothermal growth. The controllable synthesis process and possible formation mechanism were also demonstrated through a series of time-dependent experiments. The hierarchical V_2O_5/TiO_2 nanofiber catalysts were further applied in the oxidation of volatile organic compounds for the first time and were found to present high oxidation performance on acetone. The morphological, structural, chemical characterization and catalytic performance analyses illustrated the highest catalytic activity was obtained from the synthesized V_2O_5/TiO_2 nanofiber catalyst with 5 wt. % V_2O_5. This finding could be attributed to the combined effect of specific hierarchical nanofibrous morphology, abundant oxygen vacancies, and appropriate vanadium concentration.

Keywords: V_2O_5/TiO_2; electrospinning; hydrothermal; nanofibers; acetone oxidation

* *To whom correspondence should be addressed. Fax: (86)571-87951335. E-mail: xgao1@zju.edu.cn*

1 Introduction

Under the pressure of increasing environmental awareness, governments all over the world have developed stringent regulations to limit the emissions of atmospheric pollutants from automobiles and industrial activities.[1, 2] As significant atmospheric pollutants that are toxic to human health and are involved in the formation of photochemical smog,[3] volatile organic compounds (VOCs), which are emitted from vehicle exhaust, solvent evaporation, oil refining, and others, were preferentially enrolled in the blacklist of emission reduction.[4] Catalytic oxidation is one of the most efficient and cost-effective methods in removing VOCs.[5]

Noble metals and transition metal oxides have been widely studied for the catalytic oxidation of VOCs. Noble metal catalysts present excellent oxidation performance at low-temperature range,[6] but their industrial application is significantly limited by the scarcity of resources, high cost, and the characteristic of being easily degraded by Cl- or S-containing species [7]. Transition metal oxides such as Fe_2O_3,[8] Co_3O_4,[9] and V_2O_5[10] have attracted much attention. Among them, vanadium oxide has been investigated to be effective in VOC oxidation.[11, 12] In addition, V_2O_5/TiO_2 catalysts with excellent catalytic performance have been widely studied in NH_3–SCR,[13] VOC oxidation,[14] and photocatalysis.[15] Furthermore, the redox properties of V_2O_5/TiO_2 catalysts could be modified because of the electronic interaction between TiO_2 and VO_x species.[16]

Catalysts prepared via conventional methods such as wet impregnation, sol–gel, and direct calcination display certain deficiencies like declining specific surface area

and torpid mass transfer process.[17] Electrospinning is a remarkable and versatile technique for catalyst fabrication, which endows the obtained materials with controllable structures and nanofibrous morphologies that are favorable for the mass transfer process in heterogeneous catalytic reaction.[18, 19] When electrospinning is combined with hydrothermal growth, the resulting fabricated hierarchical nanofibers exhibit many merits, which leads to their extensive application in electrochemistry,[20] photocatalysis,[21] and gas sensors.[22] However, V_2O_5/TiO_2 catalysts synthesized via electrospinning combined with hydrothermal growth have not been reported. Moreover, the as-obtained V_2O_5/TiO_2 nanofiber catalysts were applied on VOC oxidation for the first time. Both synthesis methods have been proven to be comparatively versatile, low cost, applicable, and environment-friendly techniques.[20]

Hence, in the present study, a hierarchical V_2O_5/TiO_2 nanofiber catalyst was synthesized by combining the electrospinning technique and hydrothermal growth method. Moreover, the as-obtained catalysts were supposed to exhibit enhanced performance on VOC oxidation. In this study, acetone was chosen as the representative VOC because it is relatively familiar in the atmosphere. The morphological, structural, and chemical characteristics of the catalysts were investigated by SEM, TEM, XRD, Raman, EDS, N_2 adsorption, and XPS method, and the catalytic performance on acetone oxidation was also measured. These analyses were carried out to investigate the influence of the synthesis parameters on the morphological structure and acetone oxidation performance and to reveal the structure–function relationship. This study may provide guidance for the synthesis of

novel metal oxide catalysts for application in broad fields that involve filtration devices.[23-25]

2. Experimental

2.1 Catalyst preparation

The hierarchical V_2O_5/TiO_2 nanofiber catalysts were prepared by the electrospinning and hydrothermal method. This synthetic method involved the following steps： (1) electrospinning of the precursor solution to obtain primary TiO_2 nanofibers after calcination; (2) hydrothermal growth of V_2O_5 nanoparticles on TiO_2 nanofibers to obtain hierarchical V_2O_5/TiO_2 nanofiber catalyst after calcination.

Firstly, 3.0 g Polyvinylpyrrolidone (PVP, Mw=1,300,000) was dissolved in a mixed solution containing 30 ml ethanol and 10 ml acetic acid. After magnetically stirring for 1 h, 10 g tetrabutyl titanate was added into the mixed solution, and the obtained yellow titania precursor solution was further magnetically stirred overnight at room temperature. Then the viscous sol-gel solution was electrospun between a 10 ml syringe and a piece of aluminum foil attached on a roller at a rotating speed of 50 rpm. The applied voltage was 15 kV and the distance from the electrode to collector was 15 cm. The injection speed was controlled by a syringe pump at constant 1.0 ml/h. The primary TiO_2 nanofibers (denoted as pure TiO_2) were obtained after calcination in a muffle at 500 ^oC for 3 h in air.

Secondly, 0.0348 g vanadium (III) acetylacetonate and 0.60 g urea were

dissolved in 75 ml deionized water. Under the condition of magnetic stirring, 0.36 g hexadecyl trimethyl ammonium bromide (CTAB) and 0.5 ml polyethylene glycol (PEG, Mw=400) were added into the mixed solution drop by drop. Then the resulting solution was transferred into a 100 ml Teflon-lined autoclave with 100 mg primary TiO_2 nanofibers. The autoclave was sealed and heated at 120 ^oC for 24 h, and naturally cooled to room temperature. The film was collected out, washed successively three times each with ethanol and deionized water, and then dried under vacuum at 50 ^oC overnight. Then the as-obtained films were calcinated at 400 ^oC for 3h. Thus, the hierarchical V_2O_5/TiO_2 nanofibers were fabricated. This sample was denoted as V_2Ti, where the subscript is the expectant mass percentage of V_2O_5 (in wt. %). By adjusting the weight of vanadium (III) acetylacetonate added into the precursor solution proportionally, a series of V_2O_5/TiO_2 nanofibers with different V_2O_5 content were fabricated through this synthetic method, which were denoted as V_5Ti, $V_{10}Ti$ and $V_{25}Ti$, respectively.

For comparison, pure V_2O_5 powders (denoted as pure V_2O_5) were also prepared by direct calcination of ammonium metavanadate in a muffle at 500 ^oC for 3 h in air.

2.2 Catalyst characterizations

The morphology of obtained samples were characterized with thermal field-emission scanning electron microscopy (FE-SEM), recording on a SIRION-100 microscope. Energy dispersive X-ray energy dispersive spectroscopy (EDS,

GENESIS4000) combined with SEM was used to determine the element content on the surface.

Transmission electron microscopy (TEM) was performed using a Tecnai G2 F20 S-TWIN microscope operating with an acceleration voltage of 200 kV.

X-ray powder diffraction (XRD) patterns were measured on a PANalytical X'Pert PRO XRD system using Cu Kα radiation (λ=0.15418 nm) in the 2θ range between 10 and 90° at a scanning rate of 4°/min.

Raman spectra were obtained using a Raman spectrometer (LabRamHRUV, JDbin–Yvon, France) with Raman shift from 50 to 2000 cm^{-1} under the 514 nm excitation laser light. All the Raman spectra were recorded at room temperature with a resolution of 1 cm^{-1}.

The N_2 adsorption–desorption experiments were performed at liquid nitrogen temperature (77 K) using a Micromeritics Instrument Corporation (Norcross, Georgia) Accelerated Surface Area and Porosimetry (ASAP) 2020 system. The specific surface areas were calculated from the N_2 adsorption isotherms by applying the Brunauer–Emmett–Teller (BET) equation. The pore volume and average pore diameters were determined by the Barrett–Joyner–Halenda (BJH) method using the desorption branches.

X-ray photoelectron spectroscopy (XPS) were performed with a Thermo ESCALAB 250Xi using Al Kα as the radiation source at constant pass energy of 1486.6 eV. The binding energies for Ti 2p, V 2p, O 1s, C 1s were referenced to the energy of C 1s peak at 284.6 eV.

2.3 Catalytic activity

The catalytic oxidation of acetone were performed in a fixed bed tubular quartz reactor with an inner diameter of 6 mm. 50 mg of the catalyst was placed in the center of the reactor and held by glass wool. Total feed flow was kept at 300 ml/min, leading to the gas hourly space velocity (GHSV) of total feed holding at 360,000 ml/(g·h). The feed gas mixture contained 500 ppm acetone, 5% O_2, and balanced N_2. The temperatures of the catalyst bed and tubular furnace were monitored automatically by E-type thermocouples. The inlet and outlet concentrations of acetone were analyzed by a gas chromatograph (Agilent 7890A, USA) equipped with a flame ionization detector (FID) and a capillary column of HP-Innowax (Agilent, USA) operated at 60 °C. The acetone conversion ($\omega_{acetone}$) is calculated as follows:

$$\omega_{acetone} = \frac{c_{in} - c_{out}}{c_{in}} \times 100\%$$

c_{in}, c_{out} — inlet and outlet concentration of acetone.

3 Results and discussion

3.1 Morphology characterization

The morphology and microstructure of the hierarchical V_2O_5/TiO_2 nanofibers (Fig. 1) were investigated by SEM. The primary TiO_2 nanofibers with diameters

ranging from 400 nm to 600 nm interweave with one another into a compact micro network (Fig. 1A). In addition, the pristine TiO_2 nanofibers have smooth surfaces without secondary nanostructures. After the hydrothermal growth of V_2O_5 nanoparticles, the expected hierarchical nanostructures are obtained. As shown in Fig. 1B–E, the secondary V_2O_5 nanoparticles are relatively evenly distributed on the surface of the primary TiO_2 nanofibers. Moreover, the V_2O_5 nanoparticles are distributed more densely, and their sizes increase as the concentration of the precursor in the hydrothermal solution rises. In the case of V_2Ti (Fig. 1B), the V_2O_5 nanoparticles have a distinct outline and a sparse distribution. When the mass percentage increases to 10 wt.% (Fig. 1D), a layer of V_2O_5 nanoparticles with relatively regular shape and dense distribution could be clearly observed on the surface of the pristine TiO_2 nanofibers. As the concentration further increases (Fig. 1E), the V_2O_5 nanoparticles overlap with one another, eventually forming large particles and covering the pristine TiO_2 nanofibers completely.

To obtain further information about the hierarchical V_2O_5/TiO_2 nanofibers, TEM characterization was performed. Representative TEM images of V_5Ti are illustrated in Fig. 2A–B. As shown in Fig. 2A, a single nanofiber possesses a slender morphology with a diameter of approximately 400 nm. The secondary nanoparticles could be distinguished from the primary nanofibers in the high-magnification image (Fig. 2B), which reveals that a layer of secondary nanoparticles are evenly distributed on the surface of the primary nanofibers, in accordance with the results from SEM characterization. In addition, the inner-planar spacing was measured by

high-resolution TEM. As displayed in Fig. 2C, the lattice fringe spacing of 0.352 nm, which corresponds to the (101) plane of the anatase TiO_2 (JCPDS No. 21-1272), could be observed in different positions of the nanofibers. In Fig. 2D, which was taken from the interfacial region, the measured lattice fringe spacing of 0.348 nm refers to the (110) plane of shcherbinaite V_2O_5 (JCPDS No. 41-1426). To sum up, the morphology characterization results reveal that the obtained hierarchical nanofibers were composed of TiO_2 and V_2O_5 and that secondary V_2O_5 nanoparticles were successfully grown on the surface of the primary TiO_2 nanofibers.

3.2 XRD characterization

The crystalline structure and phase purity of the V_2O_5/TiO_2 nanofibers were further characterized by XRD (Fig. 3). The XRD patterns demonstrate that all the diffraction peaks could be indexed to anatase TiO_2 (JCPDS No. 21-1272), rutile TiO_2 (JCPDS No. 21-1276), and shcherbinaite V_2O_5 (JCPDS No. 41-1426).

As displayed in Fig. 3a, the detected peaks of pure TiO_2 nanofibers at 2θ = 25.3°, 36.9°, 37.8°, 38.6°, 48.0°, 53.9°, 55.1°, 62.1°, 62.7°, 68.8°, 70.3°, 75.0°, 76.0°, 82.6° correspond to the (101), (103), (004), (112), (200), (105), (211), (213), (204), (116), (220), (215), (301), and (224) planes of TiO_2, indicating the typical anatase crystal structure of TiO_2 (JCPDS No. 21-1272). In addition, the weak signal at 2θ = 27.4° demonstrates the probable undesirable formation of rutile TiO_2 (JCPDS No. 21-1276). This finding may be attributed to the high calcination temperature because the phase

transformation from anatase phase to rutile phase could occur at 500 °C.[26] After the hydrothermal growth of low-concentration vanadium precursor, the XRD patterns of V_2Ti and V_5Ti (Figs. 3b and 3c) remain the same as that of pure TiO_2 nanofibers. No diffraction peaks of new crystal species are further detected in V_2Ti and V_5Ti, which indicates that V_2O_5 are highly dispersed in the nanofibers. Nevertheless, as the concentration further increases (Figs. 3d and 3e), several new peaks appear at 2θ = 15.3°, 20.3°, 21.7°, 26.1°, 31.0°, 32.4°, 34.3°, 41.3°, 45.5°, 47.3°, 51.2°, 61.1°, which reveal the (200), (001), (101), (110), (301), (011), (310), (002), (411), (600), (020), and (321) planes of V_2O_5 and show the typical crystal structure of shcherbinaite V_2O_5 (JCPDS No. 41-1426). The diffraction peaks on behalf of V_2O_5 in $V_{25}Ti$ are stronger and sharper than that of $V_{10}Ti$, implying that vanadium oxides are better crystallized. According to Chen and co-workers,[27] metal oxides can disperse spontaneously as a monolayer on the surface of supports, which possess different utmost monolayer dispersion capacity for each metal oxide. Therefore, the increase in crystallinity might be because the high V_2O_5 concentration loaded on the surface has exceeded the utmost monolayer dispersion capacity of the primary supporter TiO_2. The spare V_2O_5 appears as crystal and gradually forms obvious nanoparticles on the surface of the nanofibers.

With the exception of the three crystalline phases detected and described above, no other crystalline phase can be found in the V_2O_5/TiO_2 hierarchical nanostructures. These results confirm that the synthesis strategy adopted successfully achieves V_2O_5/TiO_2 hierarchical nanostructures that consist of primary TiO_2 nanofibers and

secondary V_2O_5 nanoparticles.

3.3 Raman analysis

The Raman spectra of the samples are shown in Fig. 4. As illustrated in Fig. 4a, five distinct peaks are observed at approximately 143 (E_g), 199 (E_g), 395 (B_{1g}), 515 (A_{1g}), and 636 (E_g) cm^{-1}, corresponding to the characteristic Raman modes of anatase TiO_2,[28] which is consistent with the XRD results. No peaks that can be ascribed to rutile TiO_2 are shown in the spectra may be because the content of rutile TiO_2 is too low to show distinct peaks in the Raman spectra. After the hydrothermal growth of low-concentration vanadium precursor, the Raman spectra (Figs. 4b and 4c) remain the same as that of pure TiO_2 nanofibers because no new Raman bands are found. As shown in Fig. 4d, a very weak broad band centered around 286 cm^{-1}, which might arise from the vibrations of bridging V–O–V,[29] can be observed. As the concentration further increases (Fig. 4e), another two peaks are observed around 697 and 990 cm^{-1}. The weak band around 697 cm^{-1} may also refer to bridging V–O–V, whereas the sharp Raman band around 990 cm^{-1}, which reflects the ordered lattice structure of crystalline V_2O_5, may be ascribed to the vibration of the vanadyl V=O bond. Furthermore, a remarkable decrease in the intensity of the peaks that arise from anatase TiO_2 is shown in Figs. 4d and 4e, indicating the decrease in the crystallinity of the TiO_2 supporter, which is possibly caused by the interaction between the TiO_2 supporter and the loaded V_2O_5.

In summary, Raman spectra uncovered the existence of both anatase TiO_2 and shcherbinaite V_2O_5 in the hierarchical nanostructures, thereby demonstrating the successful introduction of V_2O_5 onto the primary TiO_2 nanofibers.

3.4 Porous texture and EDS characterization

The porous texture characterization results of the V_2O_5/TiO_2 nanofiber catalysts are listed in Table 1. The specific surface area of the samples decreases gradually with the increase in the concentration of vanadium ions in the hydrothermal precursor solution. For pure TiO_2 nanofibers, the specific surface area is 31.4 m^2/g, which is higher than the 19.5 m^2/g of the TiO_2 nanofibers prepared in the similar way reported by Yuan *et al.* [30] Moreover, the V_2O_5/TiO_2 nanofibers synthesized in our work display a much higher specific surface area of 26.3 m^2/g at 4.7% vanadium loading compared with the V_2O_5/TiO_2 catalysts prepared by impregnation (6.8 m^2/g at 5.0% vanadium loading), according to the literature.[31, 32] Furthermore, when the mass percentage is increased from 2 wt.% to 25 wt.%, the specific surface area decreases drastically from 27.3 m^2/g to 2.6 m^2/g, and the average pore diameter increases from 17.6 nm to 116.9 nm. This result may be attributed to the fact that the V_2O_5 nanoparticles generated from hydrothermal growth covered and occupied the pores of the primary TiO_2 nanofibers, thereby leading to the sharp decrease in specific surface area. Therefore, the catalytic oxidation performance could be a result of the mutual influence of both the vanadium content and the specific surface area.

The bulk composition of the V_2O_5/TiO_2 nanofiber catalysts was determined by EDS analysis (Table 1). The results show that the vanadium content of the obtained V_2O_5/TiO_2 nanofibers is enhanced as the concentration of the vanadium precursor increases. However, the detected contents are not entirely consistent with the expected ones. As the vanadium concentration rises, V_2O_5 in the catalyst basically increases according to the growth of mass percentage, other than V_2Ti. Therefore, in the hydrothermal process of V_2Ti, the vanadium ions in the solution were very sparse, such that they cannot form enough vanadium species on the surface of the nanofibers within 24 h.

3.5 XPS characterization

To obtain detailed information about the surface composition and chemical state of the V_2O_5/TiO_2 nanofiber catalysts, the XPS spectra of the samples with different vanadium content were obtained and are shown in Fig. 5. The measured elements in these samples are oxygen (O 1s), vanadium (V 2p), titanium (Ti 2p), and carbon (C 1s) in the binding energy from 0 eV to 1000 eV. Oxygen, vanadium, and titanium are expected from the chemical composition of the V_2O_5/TiO_2 nanofibers. The C 1s peak was used for calibration. Table 2 displays more information about the different elements on the surface of the samples, which include pure TiO_2 and pure V_2O_5.

The O 1s curves of the various samples, which can be resolved into two peaks by deconvolution, are shown in Fig. 5A. As reported, the peaks at 529.6–529.9 eV can be

assigned to lattice oxygen (denoted as O_{lat}), and the shoulder peaks at 531.2–531.5 eV can be ascribed to the active surface-adsorbed oxygen (denoted as O_{ads}).[33, 34] The active O_{ads} contents ($O_{ads}/(O_{lat} + O_{ads})$) on the surface of the V_2O_5/TiO_2 nanofiber catalysts are displayed in Table 2. For pure TiO_2 nanofibers and pure V_2O_5 powders, the O_{ads} content accounts for a small part of 13.60% and 19.13%, respectively. After introducing V_2O_5 onto the nanofiber surface, the O_{ads} content first rises to 28.35% and then gradually decreases to 18.95% with the increasing concentration of vanadium precursor in the hydrothermal solution.

The V 2p binding energy of the different catalysts is shown in Fig. 5B. As illustrated in the figure, two kinds of vanadium oxide exist on the catalyst surface. The principal peaks at 516.6–517.0 eV and 515.5–515.7 eV can be identified as V^{5+} and V^{4+}, respectively.[16] The V^{4+} contents ($V^{4+}/(V^{4+} + V^{5+})$) on the surface of different catalysts are listed in Table 2, which shows that the V^{4+} content gradually decreases from 12.30% to 11.10% with the increase in the concentration of vanadium precursor. According to Sipos and coworkers,[35] vanadium pentoxide is always oxygen deficient, and the oxygen vacancies are compensated by the excess electrons on the vanadium sites, thereby reducing the valence state from V^{5+} to V^{4+}. Thus, the decreasing V^{4+} contents may be attributed to the reduction of oxygen vacancies.

The Ti 2p binding energy of the obtained catalysts is displayed in Fig. 5C. For pure TiO_2 nanofibers, the principal peaks at 464.4 and 458.7 eV can be identified as Ti^{4+} $2p_{1/2}$ and Ti^{4+} $2p_{3/2}$, respectively. After introducing V_2O_5, both peaks move slightly toward low binding energies within 0.5 eV, suggesting that the valence

remains Ti^{4+} because the binding energy of Ti^{3+} is 1.8 eV lower.[36] This result may be ascribed to the change in the chemical environment around Ti^{4+}.

The relative contents of V on the surface, as measured by XPS, are also shown in Table 2. The results suggest that the V/(V + Ti) ratios of the nanofiber catalysts are relatively higher than that detected by EDS, demonstrating that V_2O_5 nanoparticles mainly formed on the surface of the TiO_2 nanofibers. This finding is consistent with the conclusions in the SEM and TEM analyses.

3.6 Catalytic performance

The catalytic activities of the obtained V_2O_5/TiO_2 nanofibers for the total oxidation of acetone under the conditions of acetone/oxygen molar ratio = 1/100 and GHSV = 360,000 mL/(g·h) were measured at temperatures ranging from 200 °C to 400 °C. The conversion patterns are displayed in Fig. 6, and the light-off temperature (T_{50}, acetone conversion = 50%) and the temperature near complete oxidation (T_{90}, acetone conversion = 90%) are shown in Table 1.

In the whole temperature range, pure TiO_2 nanofibers display the lowest activity among the catalysts. However, after introducing V_2O_5, the V_2Ti sample shows a remarkable increase in acetone oxidation performance. Moreover, when the mass percentage further increases to 5 wt.%, T_{50} and T_{90} are both reduced by about 90 °C compared with pure TiO_2 nanofibers, which means that the catalyst possesses better oxidation performance. However, as the vanadium content further increases, acetone

conversion goes down obviously. For instance, compared with the V_5Ti sample, the T_{50} and T_{90} of $V_{25}Ti$ increase by about 55 and 90 °C, respectively. For the pure V_2O_5 sample prepared via direct calcination method, the T_{50} and T_{90} are 315 and 385 °C, respectively, under the same reaction conditions as those of the V_2O_5/TiO_2 nanofiber catalysts. Apparently, the pure V_2O_5 sample is inferior to the V_2O_5/TiO_2 nanofibers in terms of catalytic performance, especially at a temperature below 300 °C. Based on the above results, the V_2O_5/TiO_2 nanofiber catalysts obviously perform well for the complete oxidation of acetone. Furthermore, the products detected are essentially CO_2 and H_2O, as confirmed by the estimated carbon balance of over 99%.

In summary, V_5Ti presents the best performance on acetone oxidation, and 100% conversion is achieved at approximately 320 °C. The catalytic activity over acetone conversion of the obtained catalyst follows the sequence $V_5Ti > V_{10}Ti > V_2Ti > V_{25}Ti \approx$ pure $V_2O_5 >$ pure TiO_2.

3.7 Formation mechanism

To have more insight into the actual evolution process of the hierarchical V_2O_5/TiO_2 nanofibers, a series of time-dependent experiments was performed. To verify the ultimate shape of the secondary V_2O_5 grown on the surface of the TiO_2 nanofibers, the concentration of the vanadium precursor in the hydrothermal solution was further increased to 0.06 mol/L, that is, the mole ratio of vanadium precursor to TiO_2 nanofibers was raised to 3.6:1. Fig. 7 displays the representative SEM images of

the different samples collected stepwise after 3, 6, 12, 18, and 24 h of hydrothermal reaction. As shown in Fig. 7a, the small nanoparticles nucleated on the surface of the nanofibers displayed a misty outline during the first 3 h. When reaction was extended to 6 h, the nanoparticles could be clearly observed, as shown in Fig. 7b. As the reaction time further increased to 12 h (Fig. 7c), the nanoparticles were distributed more densely, and their sizes increased. Moreover, 18 h of hydrothermal growth resulted in the overlap of nanoparticles with one another, forming a secondary layer that completely wrapped the primary TiO_2 nanofibers (Fig. 7d). In the last 6 h of hydrothermal process (Fig. 7e), two-dimensional reticular nanowalls instead of nanoparticles were grown perpendicularly on the secondary layer. Furthermore, after calcination at 400 °C for 3 h, the morphologies of the as-obtained secondary nanostructures significantly transformed from nanowalls into V_2O_5 nanobulks, as displayed in Fig. 7f.

Based on the results of the time-dependent experiments, the possible formation mechanism of the hierarchical V_2O_5/TiO_2 nanofibers is proposed and illustrated in Fig. 8. Various steps are annotated on the image. First, the primary TiO_2 nanofibers provided a negative zeta potential on the surface,[20] which attracted the trivalent vanadium cations (V^{3+}) in the solution to attach to the surfaces under the drive of electrostatic interactions. Afterwards, the reaction of V^{3+} and urea took place on the surface of the primary TiO_2 nanofibers and formed scattered nuclei.[37, 38] As the hydrothermal process continuously proceeded, the nuclei grew large and dense and finally covered the nanofiber surface, acting as the seed layer according to a similar

synthetic method reported by Kayaci *et al.* [39]. The closely and uniformly packed nuclei determined the subsequent growth kinetics, which has been well studied.[20, 40] Afterwards, the oriented attachment growth mechanism caused the subsequent growth of reticular nanowalls,[41, 42] which spread on the surface of the seed-coated TiO_2 nanofibers. Upon calcination for 4 h in air, the nanowalls decomposed gradually and finally transformed into orange V_2O_5 nanobulks.

4 Discussion

As stated above, the morphology characterization results reveal the successful hydrothermal growth of secondary V_2O_5 nanoparticles onto the surface of primary TiO_2 nanofibers, forming the pre-designed V_2O_5/TiO_2 hierarchical nanofibers, which interweave with one another into a compact micro network. The XRD results and Raman analysis further demonstrate that the as-synthesized nanofibers consist of TiO_2 and V_2O_5, and the vanadium content increases as the concentration of the precursor rises. As reported in the literature,[18] the hierarchical nanofibrous morphology is advantageous for catalytic reaction because the special nanostructure can facilitate mass transfer for ease of access of the reactant and allow more absorption inside the structure. Qin *et al.*[17] also proposed that a nanofibrous morphology could prevent the inhibition of the mass transfer process, that is, the diffusion and adsorption/desorption of reactants/products. The obtained hierarchical nanofibers are conducive to promote the diffusion of gas molecules on the surface, which is significantly important in

heterogeneous catalytic reactions, accelerating the adsorption of reactants as well as the desorption of products. In conclusion, the material generated from a synthesis strategy that combines the electrospinning technique and hydrothermal growth exhibits a special hierarchical nanofibrous morphology, which is one of the pivotal factors that can enhance the mass transfer process, as verified by the catalytic performance results that the V_2O_5/TiO_2 hierarchical nanofibers behaved more actively than V_2O_5/TiO_2 nanoparticles prepared by traditional method (Fig. S1).

Numerous literatures have demonstrated that introducing vanadium oxide into titanium-supported catalysts could endow the composite catalyst with superior catalytic oxidation performance toward VOCs.[10, 12, 16] As is reported, vanadium pentoxide is always oxygen deficient, and the resulting oxygen vacancies are compensated by the excess electrons located on vanadium sites, leading the reduction of the valence state from V^{5+} to V^{4+}.[35] Moreover, the enhanced catalytic oxidation activity benefits from the abundant presence of oxygen vacancies, which give rise to numerous surface-adsorbed oxygen (O_{ads}).[43-45] In the synthesis process of V_2O_5/TiO_2 nanofiber catalysts, the vanadium pentoxide crystal was structure defected. To retain electroneutrality, considerable oxygen vacancies appeared.[46] Afterwards, the formation of oxygen vacancies, on one hand, compelled the valence of vanadium to decrease gradually from pentavalent to tetravalent.[46] On the other hand, the gas-phase oxygen and water molecule in the atmosphere adsorbed on the surface of the catalyst under the effect of oxygen vacancies, inducing substantial surface-adsorbed oxygen, which is recognized to be the most active oxygen species that takes main responsibility for the catalytic oxidation performance.[47, 48] Accordingly, the V^{4+} contents (V^{4+}/V_{tot}) and O_{ads} contents ($O_{ads}/(O_{lat} + O_{ads})$) conformably illustrated the extraordinary significance of oxygen vacancies. As demonstrated in Table 2, after introducing V_2O_5 onto the surface of TiO_2 nanofibers, the content of oxygen vacancies revealed a significant increase, thereby exhibited better activity for acetone

oxidation compared to pure TiO_2 nanofibers, as proven by the catalytic performance results.

The analysis was further supplemented by porous texture and EDS characterization. For the V_5Ti sample that displayed the best acetone oxidation performance, the specific surface area, which has an important function in the catalytic activity of supported metal oxide catalysts,[49, 50] was slightly (1.0 m^2/g) declined compared with the highest value for V_2Ti (27.3 m^2/g). However, the vanadium content was found to be more than tripled (EDS results). Therefore, a hydrothermal process with low vanadium concentration does not have a significant effect on the specific surface area. Instead, appropriately increasing the concentration of the vanadium precursor could enhance the oxidation performance of the catalysts because vanadium oxide performs a vital role in VOC oxidation.[14, 51, 52] By contrast, further increase in vanadium concentration would lead to a rapid decline in catalytic activity, which is ascribed to the superfluous V_2O_5 nanoparticles that covered and occupied the pores of the TiO_2 nanofibers, leading to severe decrease (the minimum was 2.6 m^2/g in $V_{25}Ti$ sample) in specific surface area. For the optimal V_5Ti sample, the appropriate vanadium concentration was conducive for acetone oxidation, and the content of oxygen vacancies was maintained at a high level. In conclusion, the sample that maintained the suitable concentration of vanadium oxides and sufficient oxygen vacancies exhibited the best activity for acetone oxidation, as proven by the catalytic performance results.

To sum up, the specific hierarchical nanofibrous morphology, the abundant oxygen vacancies, and the appropriate vanadium concentration collectively determine

the admirable oxidation performance of the obtained V_2O_5/TiO_2 nanofiber catalysts, and V_5Ti sample displays the optimal catalytic activity in acetone oxidation.

5 Conclusions

A controllable method of fabricating a hierarchical V_2O_5/TiO_2 nanofiber catalyst that combined electrospinning and hydrothermal growth was proposed. The special hierarchical nanofibrous morphology was found to enhance the mass transfer process. The XPS analysis indicates that sufficient oxygen vacancies is another advantage of the as-obtained catalysts because it could induce substantial surface-adsorbed oxygen. An appropriate vanadium content of V_2O_5/TiO_2 nanofibers was also proven to benefit the catalytic performance. Among the synthetic samples, V_5Ti displayed the highest activity of acetone conversion (T_{50} = 270 °C, T_{90} = 300 °C). Accordingly, this result can be attributed to the combined effect of the specific hierarchical nanofibrous morphology, the abundant oxygen vacancies, and the appropriate vanadium content. Through the proposed synthesis strategy, a noteworthy catalyst with excellent acetone oxidation performance was successfully prepared, which is promising for applications in broad fields that involve the synthesis of novel metal oxide catalysts and paint coat of filtration devices.

Acknowledgement

This work was supported by the National Natural Science Foundation of China (Grants No.51406179 and 51125025) and the Key Innovation Team for Science and Technology of Zhejiang Province (Grant No. 2011R50017).

References

1. A. Barry and D. Corneau, *Forest Products Journal*, 2006, **56**, 38-42.
2. J. R. Woertz, K. A. Kinney, N. D. P. McIntosh and P. J. Szaniszlo, *Removal of toluene in a fungal vapor-phase bioreactor*, 1999.
3. S. F. Zuo, Q. Q. Huang, J. Li and R. X. Zhou, *Appl. Catal. B-Environ.*, 2009, **91**, 204-209.
4. C. Warneke, J. A. de Gouw, J. S. Holloway, J. Peischl, T. B. Ryerson, E. Atlas, D. Blake, M. Trainer and D. D. Parrish, *Journal of Geophysical Research-Atmospheres*, 2012, **117**.
5. S. C. Kim, S. W. Nahm, W. G. Shim, J. W. Lee and H. Moon, *Journal of Hazardous Materials*, 2007, **141**, 305-314.
6. B. Solsona, M. Perez-Cabero, I. Vazquez, A. Dejoz, T. Garcia, J. Alvarez-Rodriguez, J. El-Haskouri, D. Beltran and P. Amoros, *Chemical Engineering Journal*, 2012, **187**, 391-400.
7. W. B. Li, J. X. Wang and H. Gong, *Catal. Today*, 2009, **148**, 81-87.
8. G. Picasso, A. Quintilla, M. P. Pina and J. Herguido, *Appl. Catal. B-Environ.*, 2003, **46**, 133-143.
9. S. J. Jiang and S. Q. Song, *Appl. Catal. B-Environ.*, 2013, **140**, 1-8.
10. A. Nie, H. Yang, Q. Li, X. Fan, F. Qiu and X. Zhang, *Industrial & Engineering Chemistry Research*, 2011, **50**, 9944-9948.
11. C. Gannoun, R. Delaigle, D. P. Debecker, P. Eloy, A. Ghorbel and E. M. Gaigneaux, *Applied Catalysis A: General*, 2012, **447**, 1-6.
12. R. Delaigle, P. Eloy and E. M. Gaigneaux, *Catal. Today*, 2012, **192**, 2-9.
13. N. Y. Topsoe, H. Topsoe and J. A. Dumesic, *Journal of Catalysis*, 1995, **151**, 226-240.
14. S. Krishnamoorthy, J. P. Baker and M. D. Amiridis, *Catal. Today*, 1998, **40**, 39-46.
15. S. T. Martin, C. L. Morrison and M. R. Hoffmann, *Journal of Physical Chemistry*, 1994, **98**, 13695-13704.
16. C. Gannoun, A. Turki, H. Kochkar, R. Delaigle, P. Eloy, A. Ghorbel and E. M. Gaigneaux, *Appl. Catal. B-Environ.*, 2014, **147**, 58-64.
17. R. Qin, J. Chen, X. Gao, X. Zhu, X. Yu and K. Cen, *RSC Advances*, 2014, **4**, 43874-43881.
18. H. Bai, J. Juay, Z. Liu, X. Song, S. S. Lee and D. D. Sun, *Applied Catalysis B: Environmental*, 2012, **125**, 367-374.
19. J. B. Mu, C. L. Shao, Z. C. Guo, Z. Y. Zhang, M. Y. Zhang, P. Zhang, B. Chen and Y. C. Liu, *Acs Applied Materials & Interfaces*, 2011, **3**, 590-596.
20. H. Wang, D. Ma, X. Huang, Y. Huang and X. Zhang, *Scientific Reports*, 2012, **2**.
21. M. Shang, W. Wang, W. Yin, J. Ren, S. Sun and L. Zhang, *Chemistry – A European Journal*, 2010, **16**, 11412-11419.
22. Z. Lou, F. Li, J. Deng, L. Wang and T. Zhang, *ACS Applied Materials & Interfaces*, 2013, **5**, 12310-12316.
23. J. Li, F. Gao, L. Q. Liu and Z. Zhang, *Express Polymer Letters*, 2013, **7**, 683-689.
24. R. S. Barhate and S. Ramakrishna, *Journal of Membrane Science*, 2007, **296**, 1-8.
25. X. H. Qin and S. Y. Wang, *Journal of Applied Polymer Science*, 2006, **102**, 1285-1290.
26. N. Wetchakun, B. Incessungvorn, K. Wetchakun and S. Phanichphant, *Materials Letters*, 2012, **82**, 195-198.
27. Y. Chen and L. F. Zhang, *Catalysis Letters*, 1992, **12**, 51-62.
28. J. Y. Shen, H. Wang, Y. Zhou, N. Q. Ye, G. B. Li and L. J. Wang, *Rsc Advances*, 2012, **2**,

9173-9178.

29. I. E. Wachs, *Dalton Transactions*, 2013, **42**, 11762-11769.
30. Y. Yuan, Y. C. Zhao, H. L. Li, Y. Li, X. Gao, C. G. Zheng and J. Y. Zhang, *Journal of Hazardous Materials*, 2012, **227**, 427-435.
31. M. P. Gimeno, J. Gascon, C. Tellez, J. Herguido and M. Menendez, *Chemical Engineering and Processing*, 2008, **47**, 1844-1852.
32. C. R. Dias, M. F. Portela and G. C. Bond, *Journal of Catalysis*, 1995, **157**, 344-352.
33. X. S. Du, X. Gao, R. Y. Qu, P. D. Ji, Z. Y. Luo and K. F. Cen, *Chemcatchem*, 2012, **4**, 2075-2081.
34. X. S. Du, X. Gao, L. W. Cui, Y. C. Fu, Z. Y. Luo and K. F. Cen, *Fuel*, 2012, **92**, 49-55.
35. B. Sipos, M. Duchamp, A. Magrez, L. Forro, N. Barisic, A. Kis, J. W. Seo, F. Bieri, F. Krumeich, R. Nesper and G. R. Patzke, *Journal of Applied Physics*, 2009, **105**.
36. J. Fang, X. Z. Bi, D. J. Si, Z. Q. Jiang and W. X. Huang, *Applied Surface Science*, 2007, **253**, 8952-8961.
37. J. Livage, *Materials*, 2010, **3**, 4175-4195.
38. C. Weeks, Y. N. Song, M. Suzuki, N. A. Chernova, P. Y. Zavalij and M. S. Whittingham, *Journal of Materials Chemistry*, 2003, **13**, 1420-1423.
39. F. Kayaci, S. Vempati, C. Ozgit-Akgun, N. Biyikli and T. Uyar, *Appl. Catal. B-Environ.*, 2014, **156**, 173-183.
40. C. R. Bullen and P. Mulvaney, *Nano Letters*, 2004, **4**, 2303-2307.
41. M. Li, F. Y. Kong, H. Q. Wang and G. H. Li, *Crystengcomm*, 2011, **13**, 5317-5320.
42. L. Ren, L. Jin, J. B. Wang, F. Yang, M. Q. Qiu and Y. Yu, *Nanotechnology*, 2009, **20**.
43. Z. Y. Tian, P. H. T. Ngamou, V. Vannier, K. Kohse-Hoinghaus and N. Bahlawane, *Appl. Catal. B-Environ.*, 2012, **117**, 125-134.
44. T. Garcia, S. Agouram, J. F. Sanchez-Royo, R. Murillo, A. M. Mastral, A. Aranda, I. Vazquez, A. Dejoz and B. Solsona, *Applied Catalysis a-General*, 2010, **386**, 16-27.
45. B. de Rivas, R. Lopez-Fonseca, C. Sampedro and J. I. Gutierez-Ortiz, *Appl. Catal. B-Environ.*, 2009, **90**, 545-555.
46. Y. Wu, M. J. Forbess, S. Seraji, S. J. Limmer, T. P. Chou and G. Z. Cao, *Journal of Applied Physics*, 2001, **89**, 5647-5652.
47. R. Spinicci, M. Faticanti, P. Marini, S. De Rossi and P. Porta, *Journal of Molecular Catalysis a-Chemical*, 2003, **197**, 147-155.
48. E. M. Cordi and J. L. Falconer, *Applied Catalysis a-General*, 1997, **151**, 179-191.
49. S. J. Xiong, Y. X. Tang, H. S. Ng, X. X. Zhao, Z. L. Jiang, Z. Chen, K. W. Ng and S. C. J. Loo, *Toxicology*, 2013, **304**, 132-140.
50. G. F. He, Y. B. Cai, Y. Zhao, X. X. Wang, C. L. Lai, M. Xi, Z. T. Zhu and H. Fong, *Journal of Colloid and Interface Science*, 2013, **398**, 103-111.
51. Y. Yang, G. Yu, S. B. Deng, S. W. Wang, Z. Z. Xu, J. Huang and B. Wang, *Chemical Engineering Journal*, 2012, **192**, 284-291.
52. D. P. Debecker, R. Delaigle, P. Eloy and E. M. Gaigneaux, *Journal of Molecular Catalysis a-Chemical*, 2008, **289**, 38-43.

Figure captions

Fig 1. High-magnification and low-magnification SEM images of hierarchical V_2O_5/TiO_2 nanofibers: (A) pure TiO_2, (B) V_2Ti, (C) V_5Ti, (D) $V_{10}Ti$, (E) $V_{25}Ti$.

Fig 2. TEM images (A, B) and HRTEM images (C, D) of V_5Ti hierarchical nanofibers.

Fig 3. XRD patterns of hierarchical V_2O_5/TiO_2 nanofibers: (a) pure TiO_2, (b) V_2Ti, (c) V_5Ti, (d) $V_{10}Ti$, (e) $V_{25}Ti$.

Fig 4. Raman spectra of hierarchical V_2O_5/TiO_2 nanofibers: (a) pure TiO_2 , (b) V_2Ti, (c) V_5Ti, (d) $V_{10}Ti$, (e) $V_{25}Ti$.

Fig 5. (A) O 1s, (B) V 2p, (C) Ti 2p XPS spectra of hierarchical V_2O_5/TiO_2 nanofibers: (a) pure TiO_2 , (b) V_2Ti, (c) V_5Ti, (d) $V_{10}Ti$, (e)$V_{25}Ti$, (f) pure V_2O_5 .

Fig 6. Conversion of acetone as a function of reaction temperature. Reaction conditions: 300 ml/min feed flow, 500 ppm acetone, 5% O_2, N_2 balance, 50 mg catalyst, corresponding to a GHSV of 360,000 ml/(g·h).

Fig 7. (a-e) SEM images of hierarchical nanofibers before calcination with hydrothermal time of (a) 3 h, (b) 6 h, (c) 12 h, (d) 18 h and (e) 24 h. (f) SEM image of calcinated V_2O_5/TiO_2 nanofibers with hydrothermal time of 24 h.

Fig 8. Schematic of the formation process of hierarchical V_2O_5/TiO_2 nanofibers.

Figure

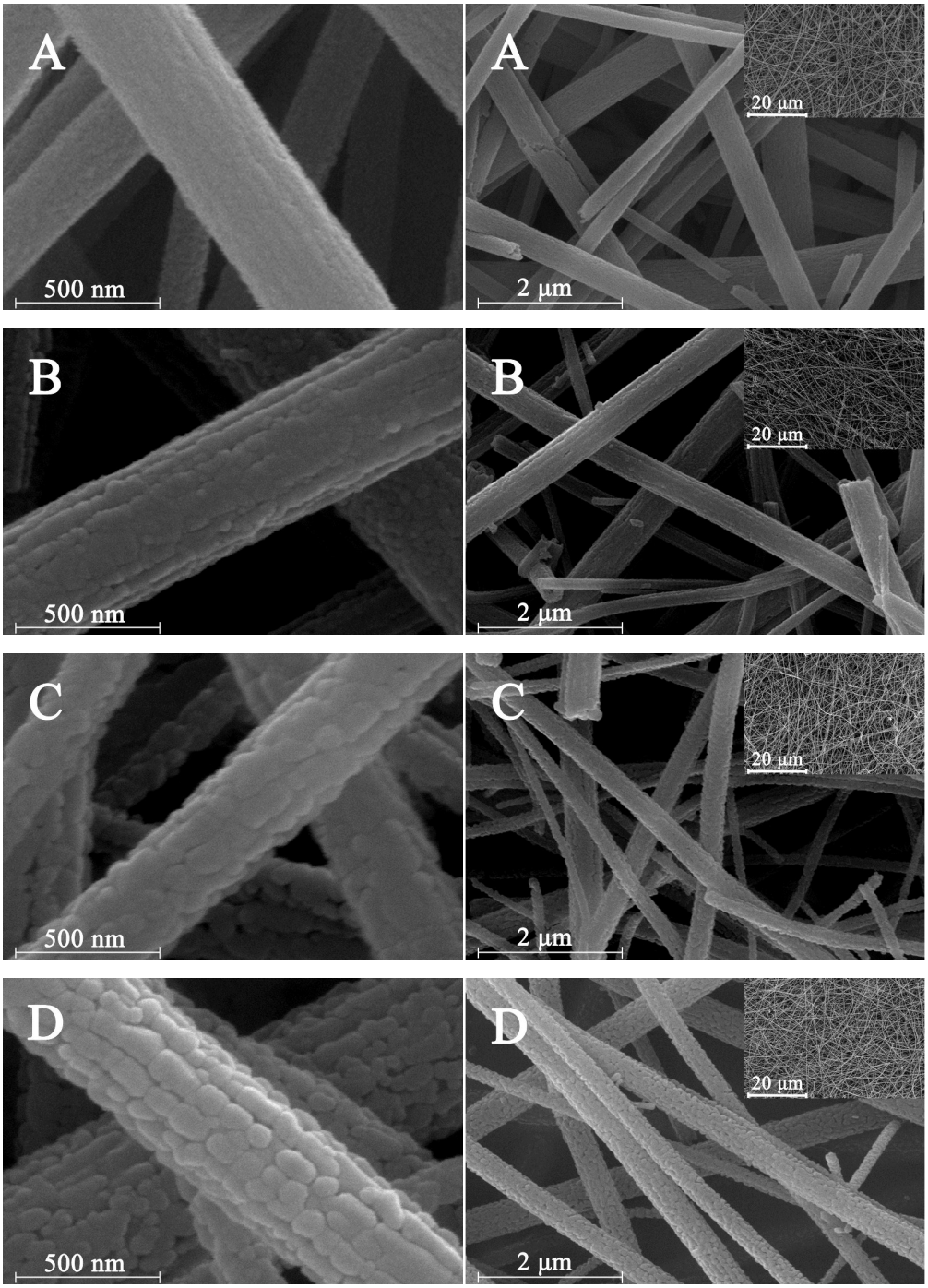

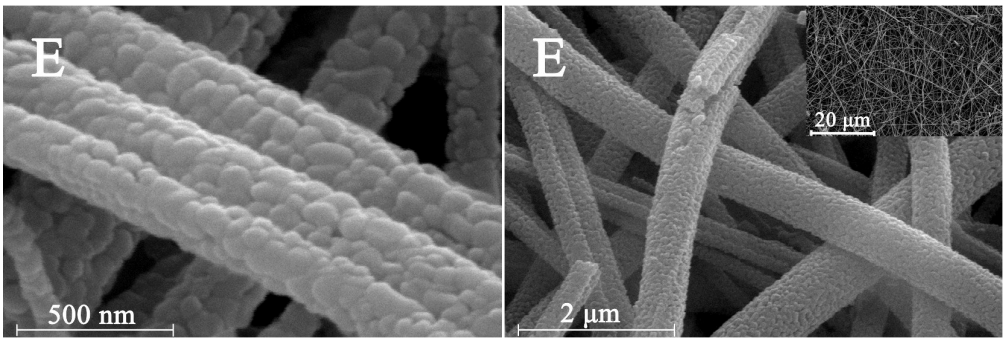

Fig 1. High-magnification and low-magnification SEM images of hierarchical V_2O_5/TiO_2 nanofibers: (A) pure TiO_2, (B) V_2Ti, (C) V_5Ti, (D) $V_{10}Ti$, (E) $V_{25}Ti$.

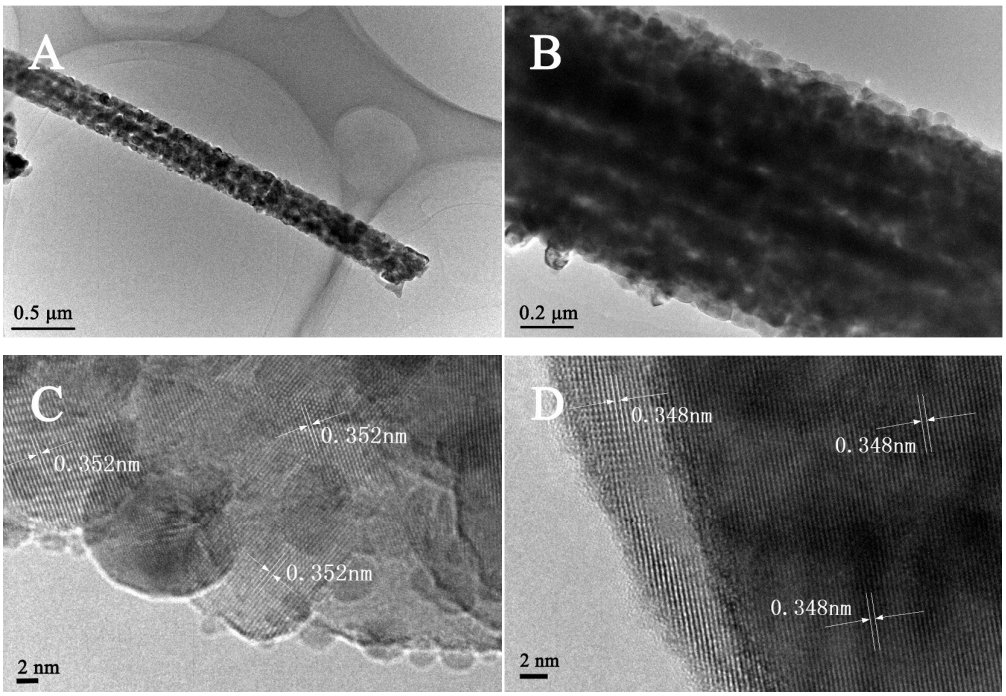

Fig 2. TEM images (A, B) and HRTEM images (C, D) of V_5Ti hierarchical nanofibers.

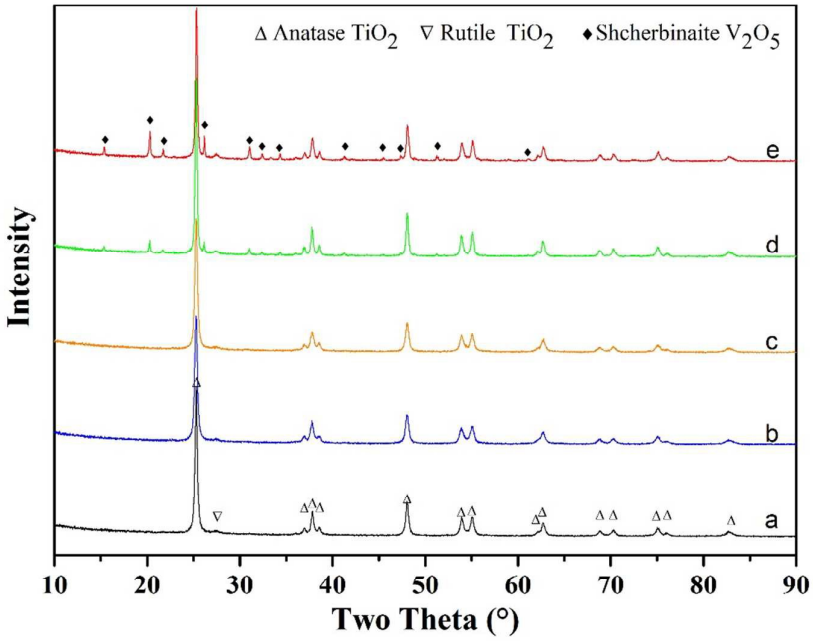

Fig 3. XRD patterns of hierarchical V_2O_5/TiO_2 nanofibers: (a) pure TiO_2, (b) V_2Ti, (c) V_5Ti, (d) $V_{10}Ti$, (e) $V_{25}Ti$.

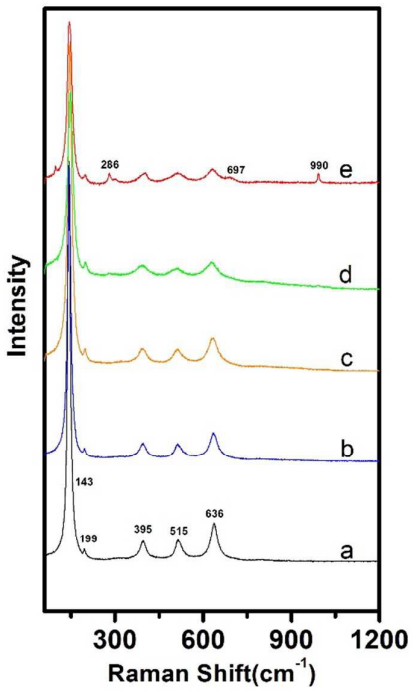

Fig 4. Raman spectra of hierarchical V_2O_5/TiO_2 nanofibers: (a) pure TiO_2 , (b) V_2Ti, (c) V_5Ti, (d) $V_{10}Ti$, (e) $V_{25}Ti$.

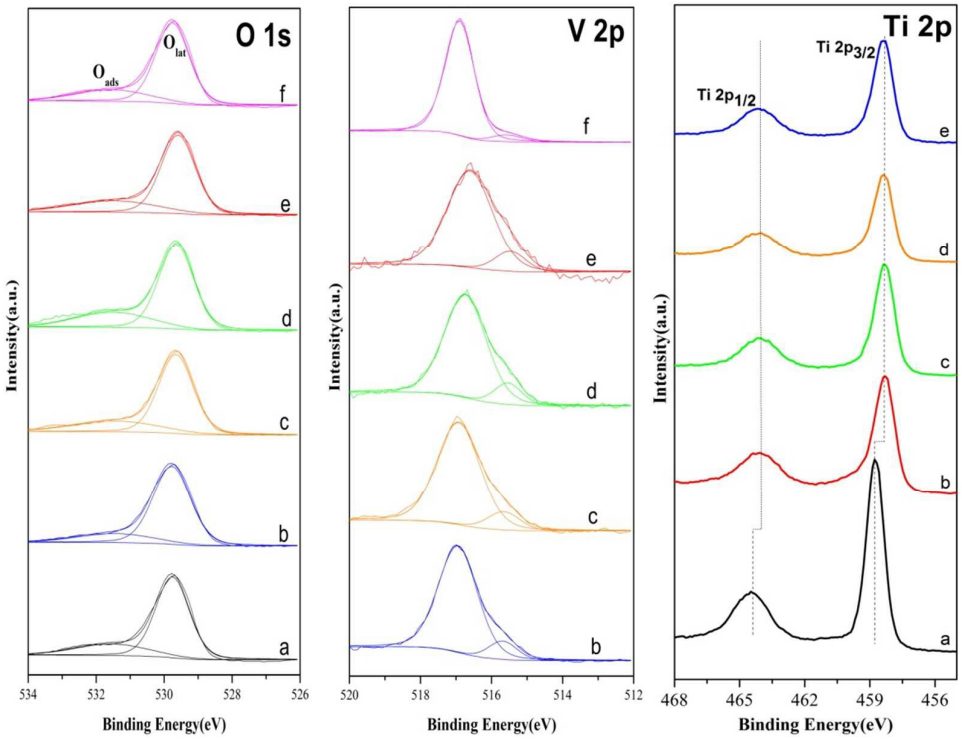

Fig 5. (A) O 1s, (B) V 2p, (C) Ti 2p XPS spectra of hierarchical V_2O_5/TiO_2 nanofibers: (a) pure TiO_2 , (b) V_2Ti, (c) V_5Ti, (d) $V_{10}Ti$, (e)$V_{25}Ti$, (f) pure V_2O_5 .

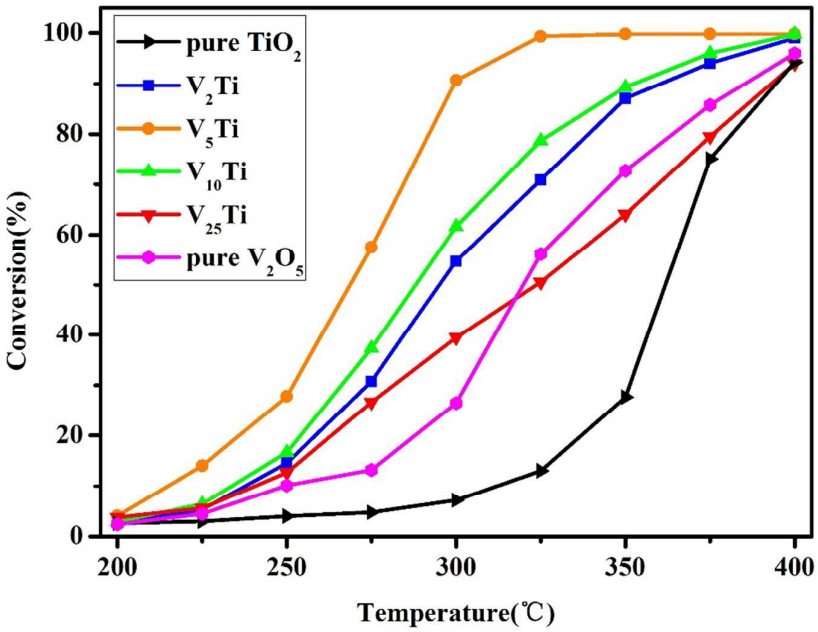

Fig 6. Conversion of acetone as a function of reaction temperature. Reaction conditions: 300 ml/min feed flow, 500 ppm acetone, 5% O_2, N_2 balance, 50 mg catalyst, corresponding to a GHSV of 360,000 ml/(g·h).

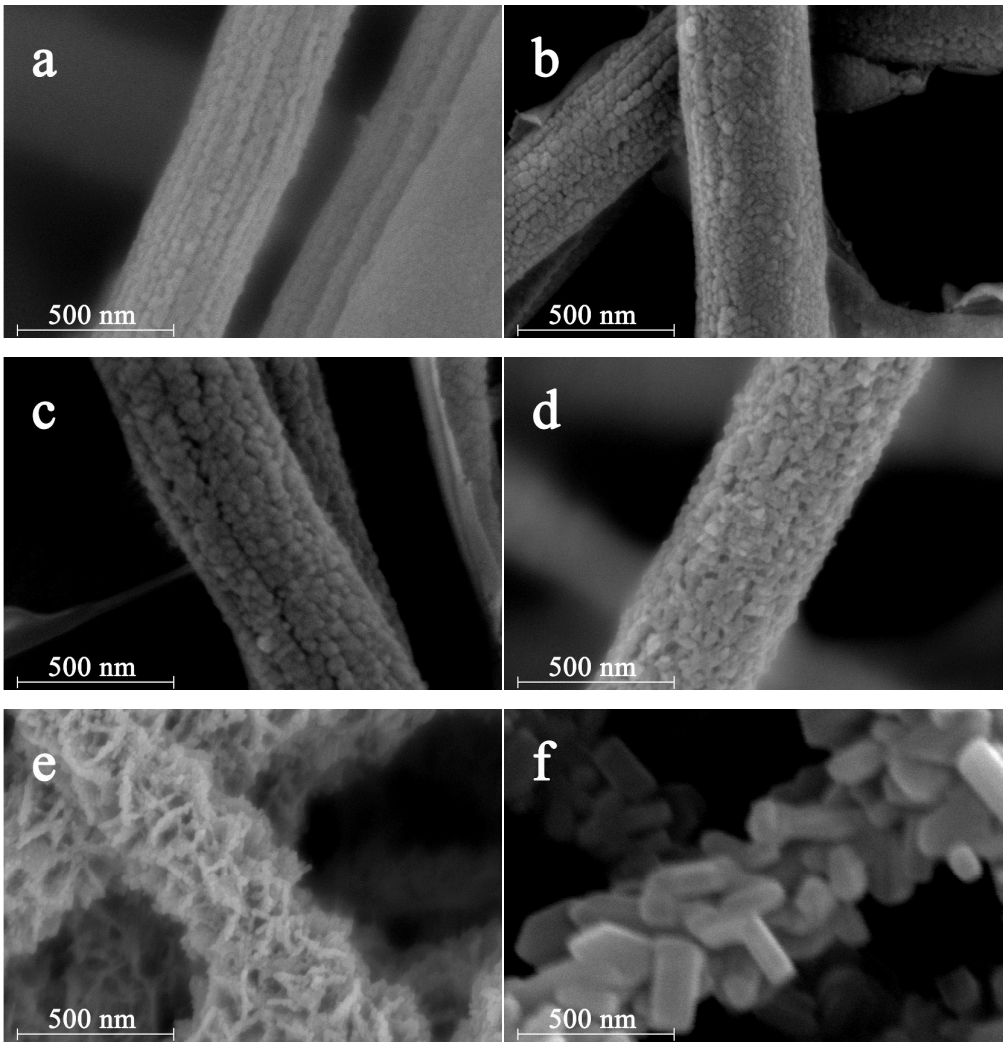

Fig 7. (a-e) SEM images of hierarchical nanofibers before calcination with hydrothermal time of (a) 3 h, (b) 6 h, (c) 12 h, (d) 18 h and (e) 24 h. (f) SEM image of calcinated V_2O_5/TiO_2 nanofibers with hydrothermal time of 24 h.

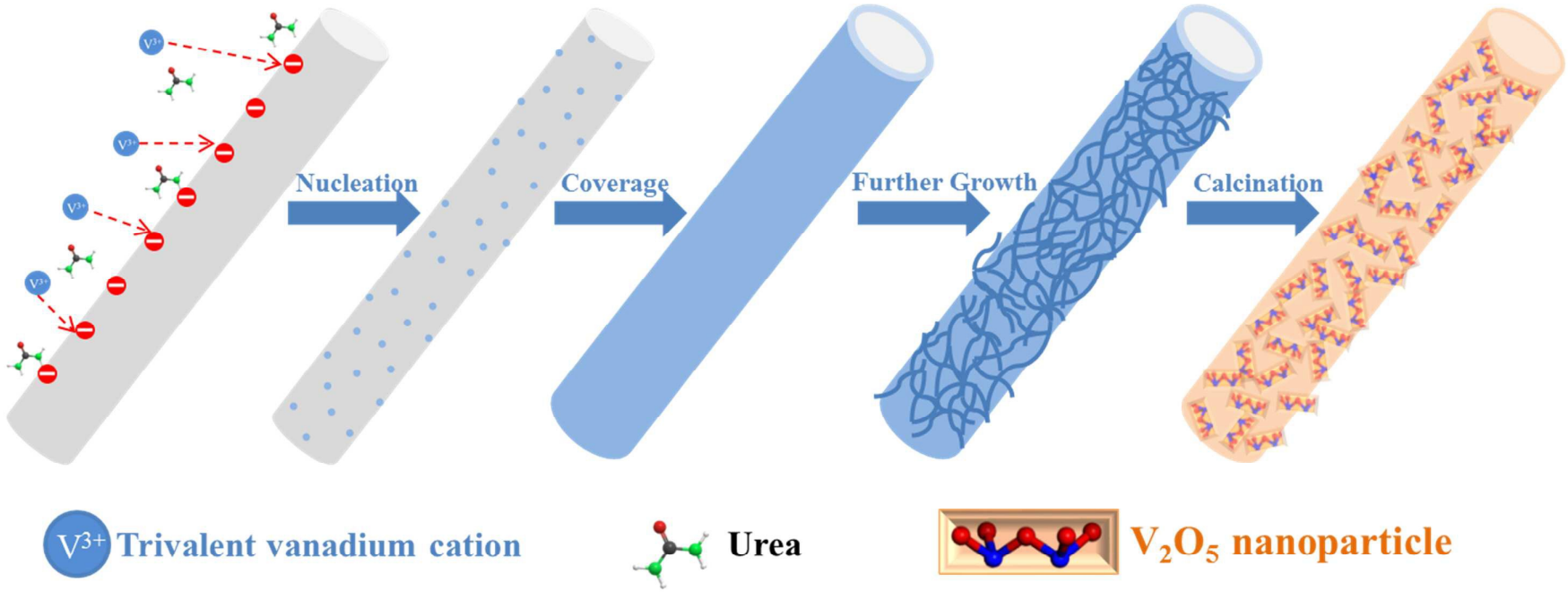

Fig 8. Schematic of the formation process of hierarchical V_2O_5/TiO_2 nanofibers.

Tab 1. Porous texture results, EDS results and catalytic performance of hierarchical V_2O_5/TiO_2 nanofibers.

Sample	Surface Area (m²/g)	Pore Volume (cm³/g)	Average Pore Diameter (nm)	V_2O_5 content (wt. %, EDS)	T_{50}(°C)	T_{90}(°C)
Pure TiO_2	31.4	0.18	23.0	0	360	390
V_2Ti	27.3	0.12	17.6	1.5	295	365
V_5Ti	26.3	0.15	22.5	4.7	270	300
$V_{10}Ti$	14.9	0.11	28.5	11.6	290	355
$V_{25}Ti$	2.6	0.08	116.9	23.1	325	390

Table 2. XPS results of hierarchical V_2O_5/TiO_2 nanofibers.

Sample	V (at. %)	Ti (at. %)	O (at. %)	V/(V+Ti) (wt. %)	$O_{ads}/(O_{lat}+O_{ads})$ (%)	$V^{4+}/(V^{4+}+V^{5+})$ (%)
Pure TiO_2	0.00	22.65	47.58	0.00	13.60	--
V_2Ti	1.13	19.68	48.52	5.76	28.35	12.30
V_5Ti	1.71	16.43	43.46	9.97	26.87	12.04
$V_{10}Ti$	2.35	14.36	43.55	14.83	26.20	11.58
$V_{25}Ti$	3.01	15.47	44.61	17.15	25.20	11.10
Pure V_2O_5	16.91	0.00	60.07	100.00	19.13	5.72